Research paper

Defect chemistry for extrinsic doping in ductile semiconductor α-Ag₂S

Hexige Wuliji [a], Kunpeng Zhao [a, *], Huirong Jing [b], Runxin Ouyang [b], Yu Yang [b],
Tian-Ran Wei [a], Hong Zhu [b, **], Xun Shi [a, c, ***]

[a] State Key Laboratory of Metal Matrix Composites, School of Materials Science and Engineering, Shanghai Jiao Tong University, Shanghai, 200240, China
[b] University of Michigan-Shanghai Jiao Tong University Joint Institute, Shanghai Jiao Tong University, Shanghai, 200240, China
[c] State Key Laboratory of High Performance Ceramics and Superfine Microstructure, Shanghai Institute of Ceramics, Chinese Academy of Sciences, Shanghai, 200050, China

ARTICLE INFO

ABSTRACT

As a new type of inorganic ductile semiconductor, silver sulfide (α-Ag₂S) has garnered a plethora of interests in recent years due to its promising applications in flexible electronics. However, the lack of detailed defect calculations and chemical intuition has largely hindered the optimization of material's performance. In this study, we systematically investigate the defect chemistry of extrinsic doping in α-Ag₂S using first-principles calculations. We computationally examine a broad suite of 17 dopants and find that all aliovalent elements have extremely low doping limits (<0.002%) in α-Ag₂S, rendering them ineffective in tuning the electron concentrations. In contrast, the isovalent elements Se and Te have relatively high doping limits, being consistent with the experimental observations. While the dopant Se or Te itself does not provide additional electrons, its introduction has a significant impact on the band gap, the band-edge position, and especially the formation energy of Ag interstitials, which effectively improve the electron concentrations by 2−3 orders of magnitudes. The size effects of Se and Te doping are responsible for the more favorable Ag interstitials in Ag₂S$_{0.875}$Se$_{0.125}$ and Ag₂S$_{0.875}$Te$_{0.125}$ with respect to pristine Ag₂S. This work serves as a theoretical foundation for the rational design of Ag₂S-based functional materials.

© 2024 The Authors. Published by Elsevier B.V. on behalf of The Chinese Ceramic Society. This is an open access article under the CC BY-NC-ND license (http://creativecommons.org/licenses/by-nc-nd/4.0/).

1. Introduction

The chemical and physical properties of a semiconductor are often directly influenced by the prevalent defects, whether intrinsic or extrinsic. Specifically, charged point defects play a vital role in determining the electrical transport properties. A dopant atom (impurity) that effectively introduces additional electrons into host materials, leading to n-type conductive behavior, is known as a donor. Conversely, a dopant that donates excess holes for p-type conduction is called an acceptor. Doping of semiconductors with acceptors and/or donors is essential for the rational design and

development of thermoelectric (TE) [1,2], photovoltaic [3], and other microelectronic devices [4], which, however, turns out to be challenging [5,6]. Certain semiconductors, such as TE materials (*e.g.* Ag-based chalcogenides) and blue light-emitting diodes (*e.g.* perovskites and nitrides), have been found to have difficult-to-adjust electrical properties through extrinsic doping [7,8]. Therefore, revealing the defect chemistry associated with doping strategies in such semiconductors is not only crucial for realizing their full potential but also for advancing their practical applications.

Silver sulfide (Ag₂S), a unique inorganic ductile semiconductor, has garnered worldwide attention due to its impressive metal-like ductility and semiconducting behaviors, which makes it highly suitable for applications in flexible and wearable electronics [9–13]. Ag₂S undergoes a phase transition from a monoclinic structure (α-Ag₂S) to a cubic structure (β-Ag₂S) at about 450 K [14]. The experimentally prepared α-Ag₂S materials exhibit n-type conduction with electron concentration of around 10¹⁴ cm⁻³ [15]. Such intrinsically low electron concentrations in pristine α-Ag₂S make its TE performance unsatisfactory. The electrical conductivity and *zT* value of undoped α-Ag₂S are only 0.1 S m⁻¹ and 6.3 × 10⁻⁵

 * Corresponding author.
 ** Corresponding author.
 *** Corresponding author. State Key Laboratory of Metal Matrix Composites, School of Materials Science and Engineering, Shanghai Jiao Tong University, Shanghai, 200240, China.
    E-mail addresses: zkp.1989@sjtu.edu.cn (K. Zhao), hong.zhu@sjtu.edu.cn (H. Zhu), xshi@mail.sic.ac.cn (X. Shi).

Peer review under responsibility of The Chinese Ceramic Society.

Please cite this article as: H. Wuliji, K. Zhao, H. Jing *et al.*, Defect chemistry for extrinsic doping in ductile semiconductor α-Ag₂S, Journal of Materiomics, https://doi.org/10.1016/j.jmat.2024.01.009

[16], respectively, at room temperature. By alloying a certain amount of isovalent Se or Te in Ag$_2$S, the electrical conductivity could be improved to 2.7 × 10^4 S/m and the *zT* value could be improved to above 0.4 at 300 K [16−19]. However, most aliovalent dopants like halogens, seems to be little or virtually non-functional in improving the electrical transport properties [20]. The relatively low doping efficiency of extrinsic n-type dopants for Ag$_2$S poses a significant challenge when attempting to enhance its electrical transport properties.

To date, only a few theoretical studies based on density functional theory (DFT) have been undertaken to elucidate the mechanism governing the electrical transport properties of α-Ag$_2$S [21,22]. Our recent work demonstrated that Ag interstitials, the most favorable one among all native defects, play a crucial role in the intrinsic n-type conduction of α-Ag$_2$S [23]. The narrow and even negative p-type dopability window suggests challenges in achieving p-type doping [23]. Hence, manipulating the Ag interstitial concentration in α-Ag$_2$S is essential for enhancing its electrical transport properties. DFT calculations for Se doped α-Ag$_2$S revealed that the formation energy of neutral Ag interstitials was decreased with increasing Se concentration [16,24]. This phenomenon could lead to an increase in electron concentration and electrical conductivity. However, the underlying mechanism behind the donor-like behavior of Ag interstitials, connected to electron concentration in isovalent Se or Te-doped Ag$_2$S alloys, remains elusive from both experimental and theoretical perspectives. Furthermore, relatively little research has been focused on defect calculations of extrinsic aliovalent doping in α-Ag$_2$S.

In this study, we thoroughly examine the defect chemistry of extrinsic doping in α-Ag$_2$S by using standard DFT methods combined with GW band-edge corrections. We have deliberately chosen 17 substitutional dopants, including isovalent elements (*e.g.* Cu, Se, Te), as well as donor-like aliovalent elements, such as alkaline earth metals, transition metals, post-transition metals, and halogens. The effect of Ag interstitials on electron concentration in the isovalent Se and Te-doped Ag$_2$S systems are also investigated. The reductions in band gaps, coupled with the reduction in formation energy of Ag interstitials in Se or Te-doped systems, lead to a significant increase in electron concentration compared to pristine α-Ag$_2$S. The analysis of Voronoi volume, chemical bonding and crystal symmetry confirms that the size effects in doped systems are responsible for the more favorable Ag interstitials compared to pristine Ag$_2$S.

2. Methods

All DFT calculations were performed using the Vienna *Ab initio* Simulation Package (VASP) code by utilizing the projector augmented wave (PAW) method [25]. The generalized gradient approximation (GGA) parameterized by Perdew, Burke and Ernzerhof (PBE) was employed for the exchange-correlation terms [26]. van der Waals (vdW) forces were accounted by incorporating the DFT-D3 correction with Becke-Johnson damping function [27]. The plane wave energy cutoff was set to 520 eV for all calculations. A rotationally invariant Hubbard *U* on-site Coulomb corrections on Ag 4d (*U* = 3 eV), Cu 3d (*U* = 7 eV) and transition metals 3d (*U* = 4 eV) orbitals were applied based on the previous studies [23,28,29]. The monoclinic structure of α-Ag$_2$S obtained from experimental reference [14] (see Fig. S1) was fully relaxed with the criteria detailed in our previous work [23].

2.1. Defect formation energies

To investigate the defect chemistry of extrinsic doping in α-Ag$_2$S, we calculate the formation energies of 17 substitutional dopants including isovalent elements (*e.g.* Cu, Se, Te) and donor-like aliovalent elements such as alkaline earth metals, transition metals, post-transition metals, and halogens. The construction of all defective supercell structures, based on the relaxed primitive cells of monoclinic α-Ag$_2$S, was accomplished using the Python charged defect toolkit (PyCDT) [30]. The total energies of both the bulk and all defect structures were computed within 3 × 2 × 2 supercells, employing the PBE combined with vdW and Hubbard *U* (denoted as PBE-vdW-*U*) method. The PyCDT method, which employs an effective and easily extendable approach known as the Interstitial Finding Tool (InFiT) [31], was used to identify all possible interstitial sites. The procedure systematically searches for potential interstitial sites using coordination pattern-recognition capabilities implemented in pymatgen [32]. Subsequently, we calculated the total energies of all possible defective configurations using DFT. Finally, we selected the most energetically favorable defective configuration, including one Ag interstitial atom, to calculate the formation energy of Ag interstitials. Comprehensive DFT calculation details can be referenced in our prior research endeavors [23]. The formation energy for a charged point defect can be calculated using [33].

$$E_{\mathrm{form}}(d, q) = E_{\mathrm{tot}}(d, q) - E_{\mathrm{tot,bulk}} + \sum_i n_i \mu_i + q(\epsilon_{\mathrm{F}} + E_{\mathrm{V}}) + E_{\mathrm{corr}}$$

(1)

where $E_{\mathrm{tot}}(d,q)$, $E_{\mathrm{tot,bulk}}$, n_i, μ_i, ϵ_{F}, E_{V} and E_{corr} are the total energy of the defected structure in charge state q, the total energy of the bulk Ag$_2$S, the number of atoms *i* added ($n_i < 0$) or removed ($n_i > 0$), the chemical potential of element *i*, the Fermi energy level referred to the valence band maximum (VBM), the VBM level, and the correction terms, respectively. The finite-size corrections were implemented using the methodology developed by Freysoldt [34] and applied through the utilization of PyCDT software. Indeed, the calculations focused solely on monocharged donors or acceptors to mitigate potential image charge errors. The single-shot quasiparticle G0W0 calculations, based on ex-ante HSE06 calculations (denoted as HSE06-G0W0), were employed to correct the band-edge levels and band gaps for Ag$_2$S, Ag$_2$S$_{0.875}$Se$_{0.125}$ and Ag$_2$S$_{0.875}$Te$_{0.125}$. The HSE06 calculations were applied based on the PBE-vdW-*U* ground state calculations. According to the calculated band-edge values from HSE06-G0W0, we applied a rigid shift to the band edges of the three compounds obtained from the PBE-vdW-*U* calculations.

In order to comprehend the influence of isovalent doping on the carrier concentration of α-Ag$_2$S, we have calculated the formation energies of Ag interstitials and vacancies within the Se and Te-doped systems. To preserve the monoclinic structures in the doped systems, the concentrations of Se and Te are restricted to 1/8 based on experimental data. Initially, we establish a 1 × 2 × 1 supercell using the primitive cell of monoclinic Ag$_2$S. Subsequently, we replace one S atom with one Se or Te atom to achieve the 1/8 concentration. Finally, a 3 × 1 × 2 supercell is reconstructed based on the fully relaxed 1 × 2 × 1 unit cell, effectively accommodating a total of 144 atoms in the 3 × 2 × 2 supercell for pure Ag$_2$S. The defective structures including intrinsic Ag interstitials and vacancies in Se or Te doped systems are constructed with considering all possible 91 configurations for Ag interstitials and 16 configurations for Ag vacancies. Subsequently, for each of them, the most

energetically stable defective structure is chosen for subsequent calculations. The defective structures with Ag interstitials are depicted in Fig. S2.

In order to elucidate the impacts of Ag interstitials for pure and Se or Te-doped Ag_2S contexts, various analyses were conducted. The Voronoi volume, continuous symmetry measure (CSM), and projected crystal orbital Hamilton populations (pCOHP) of Ag interstitials were computed using the Ovito, Pymatgen, and LOBSTER codes [32,35,36]. The Voronoi volume of a certain atom in space is the smallest volume of the polyhedron formed by perpendicular bisecting planes between the given atom and all other neighbors [37]. Each atom is enclosed by the polyhedron, and its space is allocated within it. Hence, a large Voronoi volume for an atom indicates not only a spacious environment around the atom but also a significant distance from its neighboring atoms. The CSM of the original structure is a normalized root-mean-square deviation from the closest structure exhibiting the desired symmetry [38]. It functions as a distance measure, seeking the end point not towards a preset reference structure but toward a specified symmetry requirement. When a structure possesses the desired space group symmetry (G-symmetry), the continuous symmetry measure (CSM) equals to 0. The CSM value increases as the structure deviates from the G-symmetry, reaching its maximum value. The integrated $-$pCOHP ($-$IpCOHP) values are computed within a 4 Å cutoff distance between the Ag interstitial atom and anions, as illustrated by the coordination structures shown in Fig. S3. These values are aggregated to yield an absolute value of total $-$IpCOHP, which is used to characterize the cumulative bonding effects. Moreover, band-structure calculations for both the pure Ag_2S system and the Se and Te-doped variants were executed using the HSE06 method. Additionally, an effective mass calculation from the electronic structure was performed using the Effmass code [39].

2.2. Chemical potentials

Utilizing the formula $\mu_i = \mu_i^0 + \Delta\mu_i$, the chemical potential μ_i is ascertained through the combination of the constituent *i*'s reference value in the standard phase (μ_i^0) and the deviation ($\Delta\mu_i$). In conditions of equilibrium growth, the chemical potentials need to be regulated in a way that ensures the stability of Ag_2S by preventing the precipitation of elemental substances in their pure form as well as other competitive compounds, especially when extrinsic dopants are introduced [40]. Therefore, the chemical potentials should satisfy the limitation $2\Delta\mu_{Ag} + \Delta\mu_S = \Delta H_{form}(Ag_2S)$, where $\Delta\mu_{Ag} \leq 0$ and $\Delta\mu_S \leq 0$. The chemical potentials including reference values in the standard phase and those at both Ag or S-rich conditions of Ag, S, and the dopants were calculated using the PBE functional, considering the vdW effect. The vdW effect was described by the DFT-D3 correction with Becke-Johnson damping function. The Hubbard U corrections on Ag 4, Cu 3d and transition metals 3d orbitals were applied. Additionally, we analyzed the most stable phase for each dopant under consideration. Regarding extrinsic dopants, our approach involved preventing the excessive precipitation of competing compounds, as outlined in the Supplementary Information (see Table S1).

2.3. Doping limits and carrier concentration

Using the defect formation energies as a basis, we computed the self-consistent Fermi level along with the carrier concentrations for both pure Ag_2S and the doped systems. The defect concentrations at specific temperatures were calculated through a self-consistent approach, maintaining charge neutrality [41]. This is denoted as follows:

$$\sum_{d^q}\left[qN_d e^{-E_{form}(d,q)/k_B T}\right] + p - n = 0 \tag{2}$$

where the sum runs over all defects d^q, N_d is the site concentrations where defects can emerge, k_B is the Boltzmann constant, T is the temperature, and p and n are the concentrations of holes and electrons, respectively. p and n are expressed as

$$p = \int_{-\infty}^{VBM} g(E)[1 - f(E)]dE \tag{3}$$

$$n = \int_{CBM}^{\infty} g(E)f(E)dE \tag{4}$$

where $f(E)$ is the Fermi-Dirac distribution and $g(E)$ is density of states (DOS). CBM stands for conduction band minimum. The charge neutrality equations were resolved through a numerical algorithm [42]. The DOS was obtained using the standard PBE-vdW-U method, with band edges adjusted according to HSE06-G0W0 corrections.

3. Results and discussion

3.1. Extrinsic dopants in α-Ag_2S

To achieve n-type doping in α-Ag_2S, one should theoretically consider introducing doping elements with more valence electrons compared to those of the original lattice elements to be substituted. In this work, we have chosen 17 substitutional dopants, including alkaline earth metals, transition metals, and post-transition metals, which are introduced at the Ag sites, and halogens and chalcogens that are strategically placed at the S sites. It is found that substitutional Al, Ga, Mg, Ca, Sc, Ti, V, Ni, Zn display high formation energies at both Ag-rich and S-rich conditions (See Fig. 1). At the Ag-rich condition, substitutional Co demonstrates similar donor-like traits as the intrinsic Ag interstitial (see Fig. 1c). However, at the S-rich condition, its formation energy increases to the values comparable to those of substitutional V and Zn (see Fig. 1d). At both Ag-rich and S-rich conditions, substitutional Mn at the Ag sites and halogens at the S sites exhibit similar donor-like characteristics as the intrinsic Ag interstitials (see Fig. 1). Particularly, the formation energies of substitutional Cr and Br are slightly lower than those of the intrinsic Ag interstitials. Shifting our focus to the isovalent dopants (Cu, Se, and Te), it becomes apparent that substitutional Se and Te at S sites have considerably lower formation energies, whereas substitutional Cu at Ag sites have high formation energies at both Ag-rich and S-rich conditions. These observations are consistent with the experimental findings [16$-$20,43$-$45].

Based on the formation energies of n-type dopants and isovalent dopants discussed above, we calculate the doping limits of extrinsic dopants and the electron concentrations in doped α-Ag_2S at 300 K. The results are depicted in Fig. 2. The calculated self-doping limits of Ag interstitials in pure α-Ag_2S at room temperature is $2.9 \times 10^{-4}\%$ and $6.4 \times 10^{-4}\%$ at S-rich and Ag-rich conditions, respectively. The corresponding electron concentration is 8.0×10^{14} cm^{-3} and 9.4×10^{16} cm^{-3} at S-rich and Ag-rich conditions, respectively. Among the various n-type dopants, only Mn, Co, and halogens demonstrate relatively high doping limits and slightly increased electron concentration in comparison to pristine α-Ag_2S (see Fig. 2a and b). The maximum achievable electron concentration is about 3.0×10^{17} cm^{-3} in Cl-doped Ag_2S, which, however, is still much lower than the optimal value for thermoelectrics [46]. All other n-type dopants exhibit even lower doping limits, leading to the electron concentrations primarily governed by the intrinsic Ag
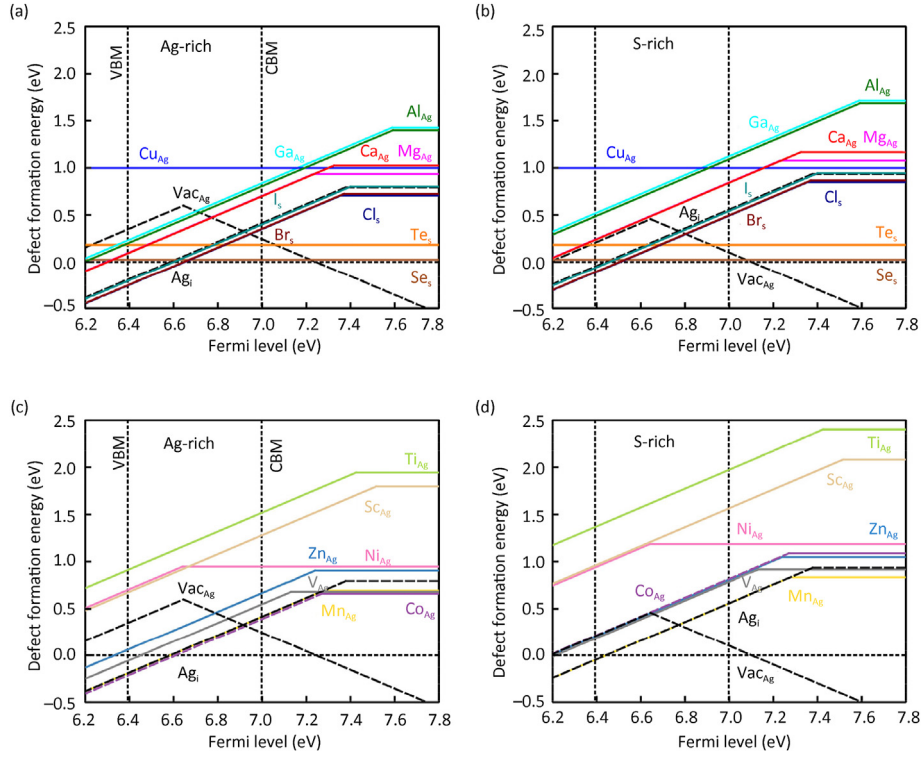
Fig. 1. Formation energies of extrinsic dopants (denoted as X_{Ag} or X_S, in this notation, "X" represents the dopants, while the subscript represents the original lattice sites that are to be replaced) as a function of Fermi energy for α-Ag$_2$S. Formation energies of isovalent elements (*e.g.* Cu, Se, Te) and donor-like aliovalent elements (including alkaline earth metals, post-transition metals, and halogens) at (a) Ag-rich and (b) S-rich conditions. Formation energies of donor-like aliovalent elements (transition metals) at (c) Ag-rich and (d) S-rich conditions. The line slope is equal to the defect charge state (+1 for donors and −1 for acceptors). The positions of VBM and CBM are denoted by the vertical dotted lines in each figure. The formation energies of intrinsic Ag interstitials (denoted as Ag$_i$) and vacancies (denoted as Vac$_{Ag}$) in pristine α-Ag$_2$S are plotted for comparison. For the sake of clarity, we categorize extrinsic dopants into two sets: (a) and (c) for Ag-rich conditions, and (b) and (d) for S-rich conditions.
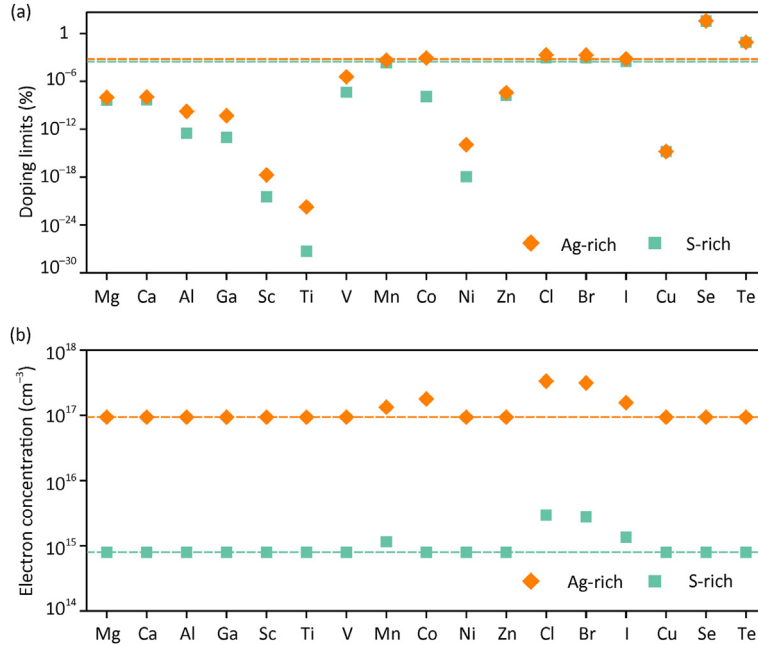
Fig. 2. (a) Doping limits of extrinsic n-type dopants in α-Ag$_2$S. The orange and green dashed lines represent the self-doping limits of intrinsic Ag interstitials at Ag-rich and S-rich conditions, respectively. (b) Electron concentration caused by extrinsic dopants and intrinsic Ag interstitials and vacancies in α-Ag$_2$S. The dashed lines represent the electron concentration caused by intrinsic defects in pristine α-Ag$_2$S. Note that the impact of extrinsic doping on intrinsic defects is not considered here. All data were computed at a temperature of 300 K.

interstitials. It is worth noting that the doping limits for isovalent dopants Se and Te are significantly higher compared to other dopants, primarily due to their relatively low formation energies. While isovalent dopants may not directly contribute excess electrons or holes to the host materials, they can still exert an influence on native defects, thereby impacting the electrical transport properties. This aspect will be furtherly explored in the upcoming section (refer to Section 3.2).

3.2. Main native defects in the Se and Te-doped Ag_2S

Based on the above analysis of extrinsic doping in α-Ag_2S, it becomes evident that the doping efficiencies of these 14 dopants are insufficient in achieving enhanced TE performance for α-Ag_2S. The efficiency of an extrinsic dopant is limited by several factors. First, the formation energy of an extrinsic dopant is the critical limiting factor, which determines the dopant solubility. If the formation energy of the dopant turns out to be high, the extra carriers provided by the dopant is insignificant compared to the intrinsic carrier concentration. Second, the formation energy of native defects may be altered due to the extrinsic doping. As a result, the concentration of free carriers resulting from native defects could be changed even if the extrinsic dopants don't provide extra carriers. Third, when the dopability window is narrow, the carriers generated by the dopant may be compensated by the native opposite carriers [47,48]. According to our previous study, intrinsic Ag interstitials function as the primary donors, whereas Ag vacancies serve as the dominant acceptors in the pristine α-Ag_2S [23]. Additionally, the results for formation energies and doping limits indicate that isovalent dopants Se and Te are the most favorable choices for α-Ag_2S compared to other dopants. Therefore, we investigate the influence of isovalent Se and Te doping on the formation of Ag interstitials and vacancies within α-Ag_2S. To maintain the monoclinic structures in the doped systems, Se and Te concentrations are limited to 1/8, as supported by experimental data. For a more detailed procedure, please refer to the Method section.

Building upon our prior research, the band gap and band-edge values play a pivotal role in defect calculations, particularly in discerning the type of carrier conduction [23]. Hence, we have computed the band gap and band-edge values for Se and Te-doped Ag_2S systems (referred to as $Ag_2S_{0.875}Se_{0.125}$ and $Ag_2S_{0.875}Te_{0.125}$), utilizing the methodology established in our prior study [23]. The obtained results are presented in Table 1. It is found that HSE06-G0W0 correction based on PBE-vdW-U method can open the gap values for $Ag_2S_{0.875}Se_{0.125}$ and $Ag_2S_{0.875}Te_{0.125}$, as documented in our previous study for pure Ag_2S [23]. The obtained band-gap values for $Ag_2S_{0.875}Se_{0.125}$ and $Ag_2S_{0.875}Te_{0.125}$ are 0.4943 eV and 0.3321 eV, respectively, both of which are lower than that of pristine Ag_2S (0.6057 eV). Moreover, after doping Se/Te in Ag_2S, the CBM level is decreased by 0.2134 eV and 0.0820 eV in $Ag_2S_{0.875}Se_{0.125}$ and $Ag_2S_{0.875}Te_{0.125}$, respectively, which is beneficial for improving electron concentration in the Se or Te doped systems compared to pure Ag_2S.

Fig. 3 illustrates the formation energies of Ag interstitials and

vacancies in the pure Ag_2S, $Ag_2S_{0.875}Se_{0.125}$ and $Ag_2S_{0.875}Te_{0.125}$. The charge state of a specific defect depends on the position of the Fermi level. Generally, the cation vacancy should exhibit acceptor-like characteristics. However, when the Fermi level is very close to or below the valence band maximum, the system is under p-type heavily doped conditions and the chemical potential of the electrons near Ag vacancy is very high [6,49,50]. Consequently, the Ag vacancy could supply electrons and exhibit donor-like characteristics. The formation energies of Ag interstitials are reduced upon Se or Te doping in Ag_2S at both Ag-rich and S-rich conditions. The alterations in band gaps, band-edge positions, and particularly the formation energies of Ag interstitials result in a downward and right shifting of the crossing point between the donor and acceptor lines in Se or Te doped systems. For example, at Ag-rich condition, the formation energy of Ag interstitial at the crossing point is 0.3295 eV for Ag_2S, which is reduced to 0.2512 eV in $Ag_2S_{0.875}Se_{0.125}$ and 0.1053 eV in $Ag_2S_{0.875}Te_{0.125}$ (see Fig. S4). Particularly, the crossing points of Se or Te doped systems have been shifted into the conduction band at Ag-rich condition. This shift makes the Fermi level move closer to the CBM and leads to an increase of electron concentration in Se or Te-doped systems.

To examine the effect of disordered atomic sites of isovalent dopants on native defect formation in the Ag_2S-based alloy, we constructed a fully disordered supercell for the $Ag_2S_{0.875}Se_{0.125}$ alloy by utilizing the special quasirandom structures (SQS) method [51,52] with the ATAT code [53]. Then we calculated the total energies for all possible configurations (586 configurations) of defective structures containing one Ag interstitial atom. As can be seen the total energy varies in large range due to the different local environments in the alloy. We further calculated the formation energies of Ag interstitials for five configurations with low total energies. As shown in Fig. 4, the formation energies of Ag interstitials of $Ag_2S_{0.875}Se_{0.125}$ alloy are lower than those in pure Ag_2S under both Ag-rich and S-rich conditions, in line with the observations in the ordered $Ag_2S_{0.875}Se_{0.125}$. Moreover, it should be noted that among the 586 configurations, the Ag interstitials near Se exhibit a low formation energy, while those situated far from Se display significantly higher formation energy. These findings support the idea that the introduction of Se or Te in Ag_2S is conducive to the formation of Ag interstitials and validate the realiability of defect caclulations based on ordered anion configuraions.

Fig. 5 displays the calculated electron concentrations for the pure Ag_2S, $Ag_2S_{0.875}Se_{0.125}$ and $Ag_2S_{0.875}Te_{0.125}$. It is found that doping Se or Te at the S sites leads to a substantial increase in the electron concentration, spanning several orders of magnitude, at both Ag-rich and S-rich conditions. At room temperature, the electron concentration of $Ag_2S_{0.875}Se_{0.125}$ reaches 2.36×10^{18} cm^{-3} and 1.16×10^{17} cm^{-3} at Ag-rich and S-rich conditions, respectively. Notably, the electron concentration of $Ag_2S_{0.875}Te_{0.125}$ even achieves 6.99×10^{19} cm^{-3} and 9.25×10^{17} cm^{-3} at Ag-rich and S-rich conditions, respectively. The obtained electron concentrations are in accord with the experimental data [9,15,16,44], confirming the reliability of our calculations. Overall, among all the extrinsic dopants explored in this study, the isovalent dopants Se and Te are proved to be more efficacious in achieving elevated electron concentrations in Ag_2S. These findings offer valuable guidance for the rational design of Ag_2S chemical analogs.

3.3. Bonding & symmetry analyses of Ag interstitials

The more favorable Ag interstitials in Se or Te-doped Ag_2S can effectively enhance the electron concentration. To investigate the structural stability of Ag interstitials in Se or Te-doped systems, we analyze the Voronoi volume of the Ag interstitial atom, the bond strength between the Ag interstitial atom and the surrounding

Table 1
VBM positions (eV) and band gaps (E_g, eV) of pure Ag_2S, $Ag_2S_{0.875}Se_{0.125}$ and $Ag_2S_{0.875}Te_{0.125}$ calculated by different methods. Note that HSE06-G0W0 corrections are applied based on the standard PBE-vdW-U methods.

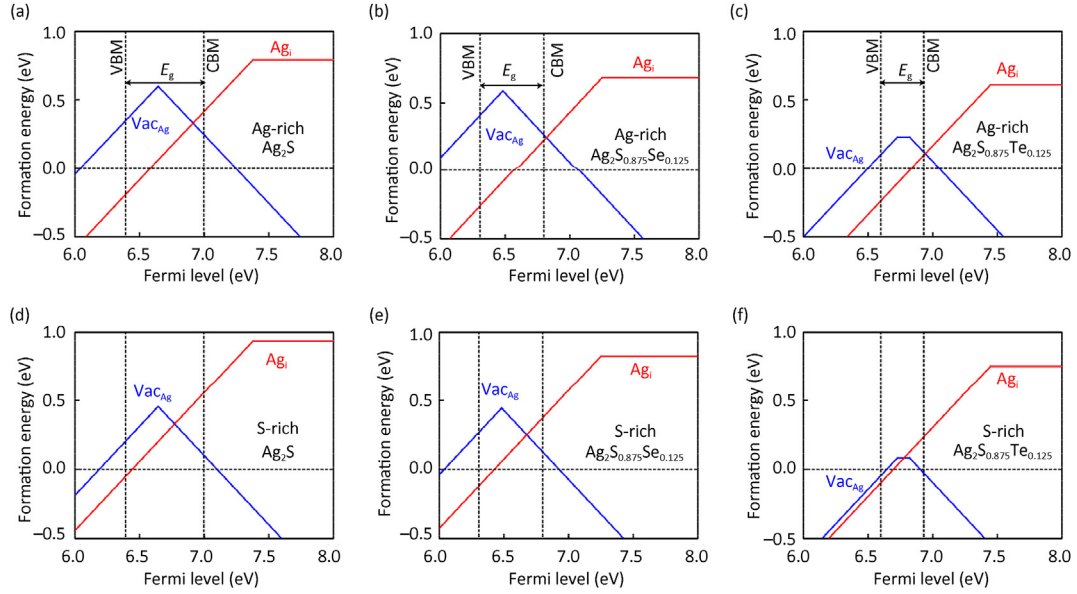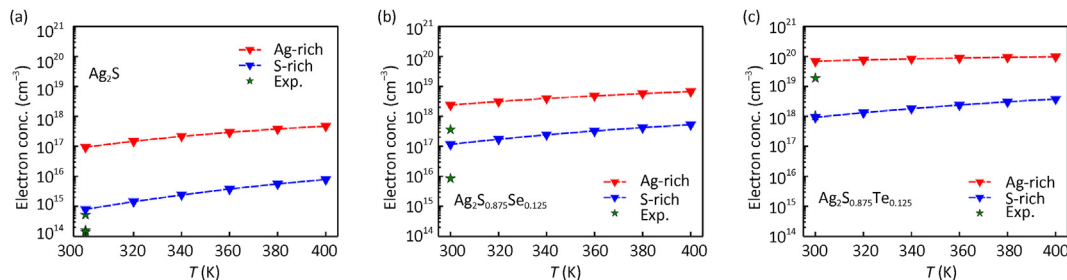| Methods	Ag_2S		$Ag_2S_{0.875}Se_{0.125}$		$Ag_2S_{0.875}Te_{0.125}$	
	E_g (eV)	VBM (eV)	E_g (eV)	VBM (eV)	E_g (eV)	VBM (eV)
PBE-vdW-U	0.0202	6.7899	0.0596	6.6584	0.0527	7.0151
HSE06-G0W0	0.6057	6.4072	0.4943	6.3052	0.3321	6.5988

H. Wuliji, K. Zhao, H. Jing et al.

Fig. 3. Formation energies of Ag interstitials and vacancies as functions of Fermi energy for pure and Se or Te-doped Ag_2S. Formation energies at the Ag-rich condition for pure Ag_2S (a), $Ag_2S_{0.875}Se_{0.125}$ (b) and $Ag_2S_{0.875}Te_{0.125}$ (c). Formation energies at the S-rich condition for pure (d), $Ag_2S_{0.875}Se_{0.125}$ (e) and $Ag_2S_{0.875}Te_{0.125}$ (f). Band gaps are denoted as E_g. Note that we didn't plot the neutral charged Vac_{Ag} for Ag_2S and $Ag_2S_{0.875}Se_{0.125}$ because its formation energy is higher than that of donor or acceptor-like Vac_{Ag}.
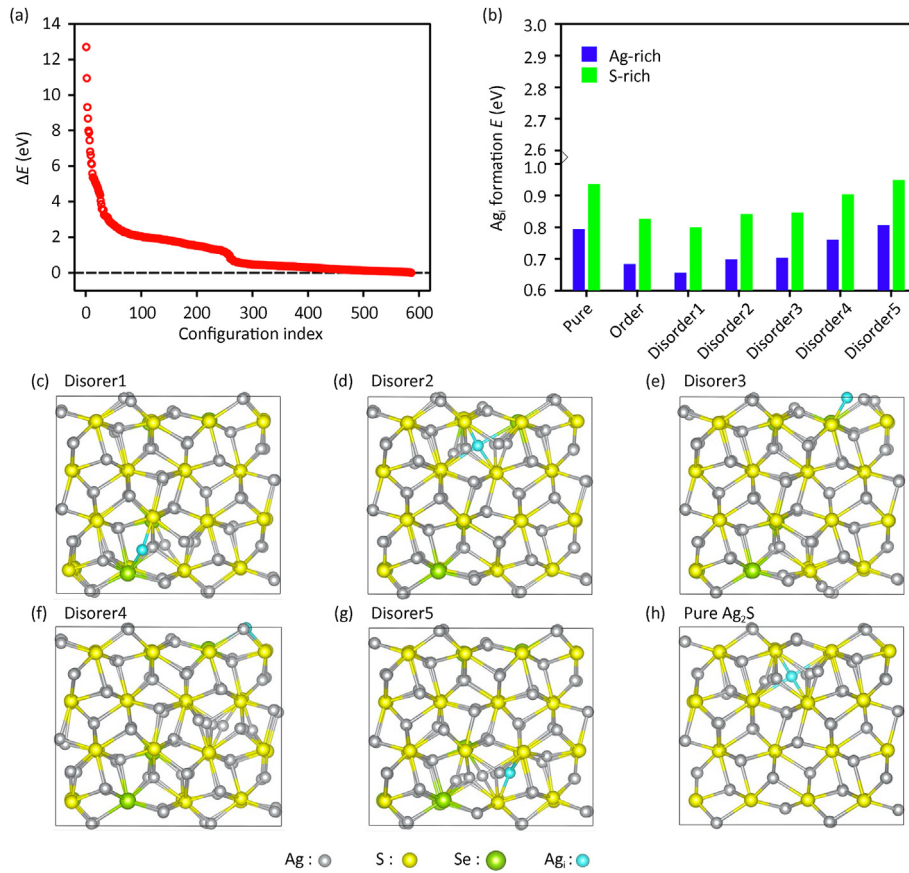

Fig. 4. (a) Total energy differences of 586 configurations for the $Ag_2S_{0.875}Se_{0.125}$ alloy with one Ag interstitial. (b) Formation energy of Ag interstitials in pure Ag_2S, ordered and disordered configurations of $Ag_2S_{0.875}Se_{0.125}$. (c–g) Five configurations of disordered $Ag_2S_{0.875}Se_{0.125}$ with one Ag interstitial atom. (h) Pure Ag_2S with one Ag interstitial atom.

anions (described by $-pCOHP$), and the local structural distortion (described by CSM) for the pure Ag_2S, $Ag_2S_{0.875}Se_{0.125}$ and $Ag_2S_{0.875}Te_{0.125}$. Notably, the doping of Se or Te into Ag_2S leads to an increase in the Voronoi volume of Ag interstitial atoms, aligning with changes in ionic radius (see Fig. 6a). The rise in Voronoi volume of the Ag interstitial atom naturally leads to an expansion of

Fig. 5. Calculated electron concentrations for pure Ag_2S (a), $Ag_2S_{0.875}Se_{0.125}$ (b), and $Ag_2S_{0.875}Te_{0.125}$ (c) as a function of temperature. The experimental data of $Ag_2S_{0.9}Se_{0.1}$, $Ag_2S_{0.7}Se_{0.3}$, and $Ag_2S_{0.8}Te_{0.2}$ are included for comparison [9,15,16,44].
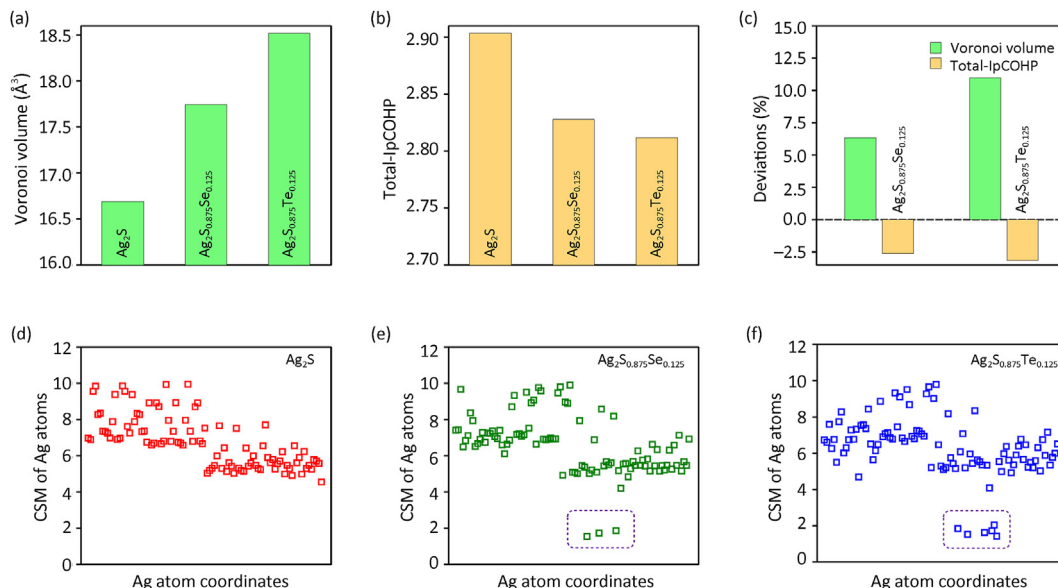
Fig. 6. Voronoi volumes of the Ag interstitial atom (a) and summation of integrated pCOHP (denoted as total $-$IpCOHP) between the Ag interstitial and the surrounding anions (b) in the $3 \times 2 \times 2$ supercells for pure Ag_2S, $Ag_2S_{0.875}Se_{0.125}$ and $Ag_2S_{0.875}Te_{0.125}$. (c) Discrepancies in Voronoi volume and total $-$IpCOHP of the Ag interstitial within $Ag_2S_{0.875}Se_{0.125}$ and $Ag_2S_{0.875}Te_{0.125}$ compared to those in pure Ag_2S. Note that IpCOHP values are counted within a cutoff distance of 4 Å between the Ag interstitial and anions. Continuous symmetry measure (CSM) of Ag atoms in defective structure with one Ag interstitial atom incorporated for (d) pure Ag_2S (red), (e) $Ag_2S_{0.875}Se_{0.125}$ (green) and (f) $Ag_2S_{0.875}Te_{0.125}$ (blue).

the distance between the Ag interstitial atom and anions. Consequently, a decreased value in the total $-$IpCOHP is observed for Se or Te-doped system compared to the pure Ag_2S (see Fig. 6b). However, the Voronoi volume increases by 6.33% in $Ag_2S_{0.875}Se_{0.125}$ and by 10.97% in $Ag_2S_{0.875}Te_{0.125}$, while the total $-$IpCOHP only decreases by 2.60% in $Ag_2S_{0.875}Se_{0.125}$ and by 3.16% in $Ag_2S_{0.875}Te_{0.125}$ (see Fig. 6c). Therefore, it can be inferred that the volume expansion induced by Se or Te doping is a crucial factor favoring the formation of Ag interstitials in doped systems. Hence, the observed size effects, representing the variation in the local atomic volume for each atom between pure Ag_2S and Se or Te-doped systems, account for the enhanced favorability of Ag interstitials. It also can be found that doping 1/8 concentration of Se in Ag_2S results in a lattice expansion for both ordered and disordered $Ag_2S_{0.875}Se_{0.125}$ compared to pure Ag_2S (Table S2). This lattice expansion enlarges the space available for interstitial sites, thereby promoting the formation of Ag interstitials. We have also calculated the Voronoi volumes for all atoms in pure Ag_2S, including 97 Ag cations and 48 anions, as well as in ordered and disordered $Ag_2S_{0.875}Se_{0.125}$. The Voronoi volumes of Se atoms in both ordered and disordered $Ag_2S_{0.875}Se_{0.125}$ are significantly

higher than those of S atoms at the corresponding sites in pure Ag_2S. Moreover, the Voronoi volume of certain Ag atoms in both ordered and disordered $Ag_2S_{0.875}Se_{0.125}$ exceed those at similar sites in pure Ag_2S, as shown in Fig. S5. The expansion of Voronoi volumes suggests an enlargement of the local space in Se-doped systems, which can facilitate the formation of Ag interstitials, consistent with our results from formation energy calculations.

The CSM calculations indicate that the introduction of an additional interstitial Ag in Ag_2S leads to structural distortions for Ag atoms at lattice sites, as depicted in Fig. S6. However, upon the introduction of extra Ag interstitials, the structural distortions of Ag atoms in $Ag_2S_{0.875}Se_{0.125}$ and $Ag_2S_{0.875}Te_{0.125}$ are slightly lower than those in pure Ag_2S (see Fig. 6d$-$f and Fig. S7). Particularly, the CSMs of certain Ag atoms in $Ag_2S_{0.875}Se_{0.125}$ and $Ag_2S_{0.875}Te_{0.125}$ (highlighted with dotted boxes in Fig. 6) are even less pronounced than those in pure Ag_2S. This phenomenon contributes to the enhanced structural stability observed in Se or Te-doped systems with Ag interstitials. It should be noted that directly observing Ag interstitial atoms in experiments is very challenging. Nevertheless, experimental results have demonstrated that the electron concentration of the system was significantly increased when Se or Te

was added to Ag_2S [16,44]. This indirectly suggests that the Ag interstitials are more favorable and the structural stability is improved in Se or Te-doped systems.

The increased favorability of Ag interstitials, coupled with the reduction in their formation energies, contributes to the enhanced electron concentrations observed in Se or Te-doped systems compared to pure Ag_2S. Moreover, we employed HSE06 method to calculate the band structures for pure Ag_2S, $Ag_2S_{0.875}Se_{0.125}$ and $Ag_2S_{0.875}Te_{0.125}$ (as shown in Fig. S8). The resulting effective masses near the CBM are nearly identical in all three compounds (as seen in Table S3). This finding suggests that doping 1/8 Se or Te at the S sites in α-Ag_2S can effectively enhance the electron concentration, while it has no impact on properties related to effective mass.

4. Conclusions

To summarize, we conducted first-principles calculations to investigate the defect chemistry associated with extrinsic doping in low-temperature α-Ag_2S. Among the 17 dopants tested, the isovalent substitution of Se and Te at the S sites exhibit notably low formation energies in α-Ag_2S. In contrast, other dopants display relatively high formation energies and rather low doping limits. Doping Se or Te into Ag_2S results in a substantial increase in electron concentration, which is primarily attributed to the reductions in band gaps, coupled with the lower formation energies and the enhanced favorability of Ag interstitials in Se and Te-doped systems. The analyses of Voronoi volume, chemical bonding and symmetry affirm that the size effect in doped systems is accountable for the heightened favorability of Ag interstitials compared to pristine Ag_2S. This study uncovers the fundamental mechanism of defect chemistry in extrinsic doping for α-Ag_2S, providing valuable insights for the strategic design of Ag_2S chemical analogs.

Declaration of competing interest

The authors declare that they have no known competing financial interests or personal relationships that could have appeared to influence the work reported in this paper.

Acknowledgements

Appendix A. Supplementary data

Supplementary data to this article can be found online at https://doi.org/10.1016/j.jmat.2024.01.009.

References

[1] Shi X, Chen L, Uher C. Recent advances in high-performance bulk thermoelectric materials. Int Mater Rev 2016;61:379−415.

[2] Zhao K, Zhu C, Zhu M, Chen H, Lei J, Ren Q, et al. Structural modularization of Cu_2Te leading to high thermoelectric performance near the Mott−Ioffe−Regel limit. Adv Mater 2022;34:2108573.

[3] Jena AK, Kulkarni A, Miyasaka T. Halide perovskite photovoltaics: background, status, and future prospects. Chem Rev 2019;119:3036−103.

[4] Gong Y, Yuan H, Wu C-L, Tang P, Yang S-Z, Yang A, et al. Spatially controlled doping of two-dimensional SnS_2 through intercalation for electronics. Nat Nanotechnol 2018;13:294−9.

[5] Van de Walle CG, Neugebauer J. First-principles calculations for defects and impurities: applications to III-nitrides. J Appl Phys 2004;95:3851−79.

[6] Seebauer EG, Kratzer MC. Charged point defects in semiconductors. Mater Sci Eng R Rep 2006;55:57−149.

[7] Wei T, Qiu P, Zhao K, Shi X, Chen L. Ag_2Q-based (Q = S, Se, Te) silver chalcogenide thermoelectric materials. Adv Mater 2023;35:2110236.

[8] Huang Y-T, Kavanagh SR, Scanlon DO, Walsh A, Hoye RLZ. Perovskite-inspired materials for photovoltaics and beyond—from design to devices. Nanotechnology 2021;32:132004.

[9] Shi X, Chen H, Hao F, Liu R, Wang T, Qiu P, et al. Room-temperature ductile inorganic semiconductor. Nat Mater 2018;17:421−6.

[10] Li G, An Q, Morozov SI, Duan B, Goddard WA, Zhang Q, et al. Ductile deformation mechanism in semiconductor α-Ag_2S. npj Comput Mater 2018;4:44.

[11] Liang X, Chen C, Dai F. Effect of plastic deformation on phonon thermal conductivity of α-Ag_2S. Appl Phys Lett 2020;117:253901.

[12] He S, Li Y, Liu L, Jiang Y, Feng J, Zhu W, et al. Semiconductor glass with superior flexibility and high room temperature thermoelectric performance. Sci Adv 2020;6:eaaz8423.

[13] Yang Q, Yang S, Qiu P, Peng L, Wei T-R, Zhang Z, et al. Flexible thermoelectrics based on ductile semiconductors. Science 2022;377:854−8.

[14] Sadanaga R, Sueno S. X-ray study on the α-β transition of Ag_2S. Mineral J 1967;5:124−43.

[15] Li L, Peng C, Chen J, Ma Z, Chen Y, Li S, et al. Study the effect of alloying on the phase transition behavior and thermoelectric properties of Ag_2S. J Alloys Compd 2021;886:161241.

[16] Liang J, Wang T, Qiu P, Yang S, Ming C, Chen H, et al. Flexible thermoelectrics: from silver chalcogenides to full-inorganic devices. Energy Environ Sci 2019;12:2983−90.

[17] Liang J, Qiu P, Zhu Y, Huang H, Gao Z, Zhang Z, et al. Crystalline structure-dependent mechanical and thermoelectric performance in $Ag_2Se_{1−x}S_x$ system. Research 2020;2020:6591981.

[18] Hu H, Wang Y, Fu C, Zhao X, Zhu T. Achieving metal-like malleability and ductility in $Ag_2Te_{1−x}S_x$ inorganic thermoelectric semiconductors with high mobility. Innovation 2022;3:100341.

[19] Wang Y, Li A, Hu C, Fu C, Zhu T. Reversible room temperature brittle-plastic transition in $Ag_2Te_{0.6}S_{0.4}$ inorganic thermoelectric semiconductor. Adv Funct Mater 2023;33:2300189.

[20] Liu J, Xing T, Gao Z, Liang J, Peng L, Xiao J, et al. Enhanced thermoelectric performance in ductile Ag_2S-based materials via doping iodine. Appl Phys Lett 2021;119:121905.

[21] Ngoc Nam H, Yamada R, Okumura H, Nguyen TQ, Suzuki K, Shinya H, et al. Intrinsic defect formation and the effect of transition metal doping on transport properties in a ductile thermoelectric material α-Ag_2S: a first-principles study. Phys Chem Chem Phys 2021;23:9773−84.

[22] Wuliji H, Ma Y, Chen H, Wei T-R, Zhao K, Sun Y-Y, et al. Dynamical approach to the atomic and electronic structures of the ductile semiconductor Ag_2S. J Chem Phys 2023;158:244109.

[23] Wuliji H, Zhao K, Cai X, Jing H, Wang Y, Huang H, et al. Study of the defect chemistry in Ag_2Q (Q = S, Se, Te) by first-principles calculations. Mater Today Phys 2023;35:101129.

[24] Nam HN, Suzuki K, Masago A, Nguyen TQ, Shinya H, Fukushima T, et al. A first-principles study on the electrical conductivity of $Ag_2S_{1−x}Se_x$ (x = 0, 0.25, 0.5): electron−phonon coupling. Appl Phys Lett 2022;120:143903.

[25] Kresse G, Furthmüller J. Efficiency of ab-initio total energy calculations for metals and semiconductors using a plane-wave basis set. Comput Mater Sci 1996;6:15−50.

[26] Perdew JP, Burke K, Ernzerhof M. Generalized gradient approximation made simple. Phys Rev Lett 1996;77:3865−8.

[27] Grimme S, Ehrlich S, Goerigk L. Effect of the damping function in dispersion corrected density functional theory. J Comput Chem 2011;32:1456−65.

[28] Jiang H, Gomez-Abal RI, Rinke P, Scheffler M. First-principles modeling of localized d states with the G W @ LDA + U approach. Phys Rev B 2010;82: 045108.

[29] Wu X, Ming C, Gao W, Shi J, Zhao K, Wang H, et al. Effect of liquidlike cations on electronic and defect properties of solid solutions of Cu_2Te and Ag_2Te. Phys Rev B 2022;105:195206.

[30] Broberg D, Medasani B, Zimmermann NER, Yu G, Canning A, Haranczyk M, et al. PyCDT: a Python toolkit for modeling point defects in semiconductors and insulators. Comput Phys Commun 2018;226:165−79.

[31] Zimmermann NER, Horton MK, Jain A, Haranczyk M. Assessing local structure motifs using order parameters for motif recognition, interstitial identification, and diffusion path characterization. Front Mater 2017;4:34.

[32] Ong SP, Richards WD, Jain A, Hautier G, Kocher M, Cholia S, et al. Python Materials Genomics (pymatgen): a robust, open-source python library for materials analysis. Comput Mater Sci 2013;68:314−9.

[33] Freysoldt C, Grabowski B, Hickel T, Neugebauer J, Kresse G, Janotti A, et al. First-principles calculations for point defects in solids. Rev Mod Phys 2014;86: 253−305.

[34] Freysoldt C, Neugebauer J, Van de Walle CG. Fully *Ab Initio* finite-size corrections for charged-defect supercell calculations. Phys Rev Lett 2009;102:

016402.

[35] Stukowski A. Visualization and analysis of atomistic simulation data with OVITO—the Open Visualization Tool. Model Simulat Mater Sci Eng 2010;18: 015012.

[36] Nelson R, Ertural C, George J, Deringer VL, Hautier G, Dronskowski R. LOB-STER: local orbital projections, atomic charges, and chemical-bonding analysis from projector-augmented-wave-based density-functional theory. J Comput Chem 2020;41:1931—40.

[37] Senthil Kumar V, Kumaran V. Voronoi cell volume distribution and configurational entropy of hard-spheres. J Chem Phys 2005;123:114501.

[38] Pinsky M, Avnir D. Continuous symmetry measures. 5. The classical polyhedra. Inorg Chem 1998;37:5575—82.

[39] Effmass D Whalley L. An effective mass package. J Open Source Softw 2018;3: 797.

[40] Lany S. Semiconductor thermochemistry in density functional calculations. Phys Rev B 2008;78:245207.

[41] Doak JW, Michel KJ, Wolverton C. Determining dilute-limit solvus boundaries in multi-component systems using defect energetics: Na in PbTe and PbS. J Mater Chem C 2015;3:10630—49.

[42] Buckeridge J. Equilibrium point defect and charge carrier concentrations in a material determined through calculation of the self-consistent Fermi energy. Comput Phys Commun 2019;244:329—42.

[43] Yang S, Gao Z, Qiu P, Liang J, Wei T, Deng T, et al. Ductile $Ag_{20}S_7Te_3$ with excellent shape-conformability and high thermoelectric performance. Adv Mater 2021;33:2007681.

[44] Peng L, Yang S, Wei T-R, Qiu P, Yang J, Zhang Z, et al. Phase-modulated mechanical and thermoelectric properties of $Ag_2S_{1-x}Te_x$ ductile semiconductors. J Materiomics 2022;8:656—61.

[45] Li Z, Zhang J, Wang S, Dong Z, Lin C, Luo J. Low-temperature structure and thermoelectric properties of ductile $Ag_2S_{0.4}Te_{0.6}$. Scripta Mater 2023;228: 115313.

[46] Snyder GJ, Toberer ES. Complex thermoelectric materials. Nat Mater 2008;7: 105—14.

[47] Toriyama MY, Qu J, Snyder GJ, Gorai P. Defect chemistry and doping of BiCuSeO. J Mater Chem A 2021;9:20685—94.

[48] Gao H, Zhao K, Wuliji H, Zhu M, Xu B, Lin H, et al. Adaptable sublattice stabilized high-entropy materials with superior thermoelectric performance. Energy Environ Sci 2023;16:6046—57.

[49] Puska MJ, Pöykkö S, Pesola M, Nieminen RM. Convergence of supercell calculations for point defects in semiconductors: vacancy in silicon. Phys Rev B 1998;58:1318—25.

[50] Chen S, Yang J-H, Gong XG, Walsh A, Wei S-H. Intrinsic point defects and complexes in the quaternary kesterite semiconductor Cu_2ZnSnS_4. Phys Rev B 2010;81:245204.

[51] Zunger A, Wei S-H, Ferreira LG, Bernard JE. Special quasirandom structures. Phys Rev Lett 1990;65:353—6.

[52] Qu J, Balvanz A, Baranets S, Bobev S, Gorai P. Computational design of thermoelectric alloys through optimization of transport and dopability. Mater Horiz 2022;9:720—30.

[53] van de Walle A, Asta M, Ceder G. The alloy theoretic automated toolkit: a user guide. Calphad 2002;26:539—53.

Hexige Wuliji is a Ph.D. candidate at School of Materials Science and Engineering (SMSE), Shanghai Jiao Tong University (SJTU). He received his B.S. degree (2013) and M.S. degree (2016) in materials science and engineering from Harbin Institute of Technology. His current research mainly focuses on the investigation of structural properties, defect chemistry and transport mechanism of advanced thermoelectric materials by first-principles.

Kunpeng Zhao is currently an Associate Professor at School of Materials Science and Engineering (SMSE), Shanghai Jiao Tong University (SJTU). He received his B.S. degree (2012) from Xiamen University and Ph.D. degree (2018) from University of Chinese Academy of Sciences. His research interests mainly focus on the design, fabrication, and tailoring of advanced thermoelectric materials.

Hong Zhu is an Associate Professor at SJTU. She received her B.S. degree (2007) in SJTU and Ph.D. degree (2012) in University of Connecticut. She worked at Massachusetts Institute of Technology as a postdoctor from 2012 to 2015. Her current research focuses on advanced materials design based on atomistic scale simulations and machine learning.

Xun Shi is a Professor at Shanghai Institute of Ceramics, Chinese Academy of Science (SICCAS) and at SJTU. He received his B.S. degree (2000) in Tsinghua University and Ph.D. degree (2005) in the University of Chinese Academy of Sciences. He worked at the University of Michigan (USA) as a postdoctor from 2007 to 2009. He then joined the R&D center in General Motors. Since 2010 he has been a professor at SICCAS. His current research focuses on advanced thermoelectric materials and devices, and flexible semiconductors.